THz Imaging to Map the Microporosity Distribution in Carbonate Rocks

Shannon L. Eichmann[1,*ǂ], *Jacob* Bouchard[2ǂ], *Hooisweng* Ow[3], *Doug* Petkie[2], and *Martin* Poitzsch[3]
[1]Aramco Research Center – Houston, Aramco Services Company, Houston, TX
[2] Department of Physics, Worcester Polytechnic Institute, Worcester, MA
[3]Aramco Research Center – Boston, Aramco Services Company, Boston, MA
ǂ Contributed equally to this work.

Abstract. Terahertz (THz) spectroscopy is a non-destructive tool used in many industries to analyze materials including measuring the water content and the distribution of water in biological samples. THz Time-Domain Spectroscopy (THz-TDS) measures the dielectric and structural properties of a sample by probing it with an ultrafast THz pulse and measuring the change in amplitude and phase. In this study we demonstrate the use of THz-TDS imaging to quickly map lateral variations in microporosity (ϕ_μ) using the THz attenuation due to water in the pores after clearing the large pores via centrifugation. Three carbonate rock samples with differing ϕ and pore size distributions were selected for this study. Three water saturation states were produced for each sample: saturated, centrifuged, and dry. At each saturation state, the sample is weighed and imaged using THz-TDS to spatially map and measure ϕ_μ. The results show that for each sample the ϕ_μ obtained using THz-TDS imaging is in excellent agreement with that obtained from both mass balance and MICP. In addition, the THz-TDS maps show significant differences in the spatial distribution of the microporosity for samples having similar composition. This method provides a means to measure ϕ and ϕ_μ while mapping the spatial distribution of ϕ_μ toward improved petrophysical characterization of carbonate reservoir rocks.

1 Introduction

Carbonate reservoirs hold up to 60% of the global petroleum reserves and contain a wide range of pore types and sizes which are non-uniformly distributed compared to sandstone reservoirs where the pores have a narrow pore size distribution (PSD) and are more uniformly distributed throughout the rock matrix [1, 2]. A suite of reservoir characterization methods covering the kilometer to nanometer length scales is required to guide production and reservoir management decisions. Of particular interest for carbonate reservoirs, is the amount of microporosity (ϕ_μ) (i.e., percentage of pores <1 μm diameter) and its distribution within the rock as these pore sizes are commonly linked to the residual and bypassed oil following primary and secondary depletion [3-7].

Using laboratory analyses, geologists and engineers gain an understanding of how the rock properties (i.e., porosity (ϕ), permeability, PSD, wettability, etc.) change with depth [8-10]. Typical methods of measuring ϕ include mercury intrusion, optical and scanning electron microscopy (SEM), computed tomography (CT), and gas porosimetry [2, 10-15]. While accurate, non-imaging methods may be destructive or make use of hazardous materials to provide bulk measurements of ϕ. Imaging methods, however, can be limited by a trade-off between field-of-view (FOV) and resolution to produce ϕ distribution maps.

X-Ray CT, optical microscopy, and SEM are common imaging methods used to evaluate ϕ and PSD in conventional and unconventional reservoir rocks. CT and micro-CT provide 3D images of whole core and core plugs at 100s to 10s of microns/pixel resolution. The resolution provided by CT and even micro-CT can be insufficient to effectively map ϕ_μ distributions in carbonate rocks. In some examples, heavy ion tracers have been used to dope imbibed fluids to track fluid mobility including forced displacement and diffusion within unresolved ϕ using x-ray CT [16, 17]. Petrography using optical and fluorescence microscopy provide resolutions ranging from a few hundred nanometers up to 10s of microns [3, 18-21]. These techniques are quite versatile and through detailed analyses geologist can provide information about mineralogy, depositional environment, ϕ and PSD. SEM provides the highest resolution of these imaging techniques, down to a few nanometers/pixel, where both 2D and 3D rock images can be produced, and ϕ and PSD be measured using image processing methods. While large tiled 2D SEM (pores larger than ~5 nm) and laser scanning confocal microscopy (pores larger than ~200 nm) images can be produced to maintain high resolution while maintaining the ability to image a plug face, these images are typically very large and challenging process leading to slow turnaround time between data collection and quantification.

* Corresponding author: shannon.eichmann@aramcoamericas.com

Terahertz (THz) time-domain spectroscopy (TDS) is a relatively new method with significant development in the past 30 years [22-25]. THz-TDS operates over the 100 GHz (~30 μm) to 10 THz (~3 mm) bandwidth where the spectrometer produces a THz pulse which transmits through the sample and different proportions of the pulse are scattered, reflected, absorbed, or transmitted depending on the material properties. A Fourier transform of the transmitted time-dependent signal provides the absorbed and scattered frequencies in the spectrum. This method has been used for the investigation of chemicals [26], restoration of artwork [27] [28], water content of tissues and plants [29-31], and imaging for security applications [32]. Previous work established that THz TDS is capable of measuring bulk porosity [33, 34]. More specifically measuring ϕ and ϕ_μ of carbonates by making use of the strong water absorption in the THz spectrum and its change during dehydration [14]. This prior study, however, did not demonstrate the ability to map the ϕ_μ distribution which is relevant to reservoir characterization.

As the field of THz spectroscopy has matured, turnkey benchtop setups have been made available that greatly simplify the application of this technique. By utilizing a turnkey system, THz TDS could be integrated into a core analysis workflow with very little difficulty. In this paper we demonstrate a method of using THz TDS of carbonate rocks at different water saturation states to generate 2D ϕ_μ maps. These maps show spatial variations in the ϕ_μ within each sample and allow comparisons of these distributions between samples. These micropores and their distribution are challenging or impossible to resolve at a large FOV with most core imaging techniques. The results show that when the THz TDS ϕ_μ map data are combined with mass balance, the relative amount of microporosity in each sample can be estimated and agree well with bulk measurements.

2 Materials and Methods

2.1 Samples

Three carbonate core plug samples 1.5" in diameter were used: one carbonate plug from a field (Sample 1) and two Indiana limestone core plugs from Kocurek Industries (Caldwell, TX) (Samples 2 and 3). Samples 2 and 3 were cut into 2 mm, 4 mm, and 6 mm thick wafers and Sample 1 was cut into 2 mm and 4 mm thick wafers which were then cut in half to produce half-moon shaped samples for THz TDS imaging. The remaining half plug of each sample was used for additional characterization. Each half-moon sample was pre-cleaned to remove any pore occluding dust from the cutting process by submerging the sample in water under vacuum for two days. The sample was then centrifuged and dried in an oven at 100 °C.

2.2 Terahertz Time Domain Spectroscopy (THz-TDS)

Terahertz time domain spectroscopy (THz TDS) probes samples with short pulses of terahertz radiation and the system monitors the amplitude and phase of the transmitted pulse. The small THz wavelengths can probe small features and interact with water molecules (Figure 1a). Water strongly absorbs THz radiation, thus intensity maps from the peak-to-peak pulse amplitude at collected at 0.5 mm/pixel across samples at different saturation states correspond to the water distribution in a sample (Figure 1b). A Toptica Teraflash system equipped with an imaging gantry extension was used to measure the peak-to-peak pulse amplitude over a 70 ps window with two measurements taken at each point and averaged together.

Porosity maps were generated from three intensity maps of the same sample at different saturation states: a) fully saturated, b) centrifuged to partial saturation, and c) dried. The maps are compared using a custom image analysis script written for IgorPro to algin the sample within each map, compare the intensity at each pixel, and generate porosity maps. The map of the saturated ϕ was generated by comparing maps (a) and (c), the map of the ϕ_μ was generated from maps (b) and (c), and the map of macroporosity (ϕ_M) was generated from (a) and (b).

2.3 Workflow

Half-moon samples were measured in sequence using the workflow shown in Figure 1c. The dry sample was weighed to obtain the initial dry mass, $m_{dry,i}$, and then vacuum saturated for two days in the ion-saturated solution remaining from the pre-cleaning step to reduce calcium carbonate dissolution due to its solubility in water. The saturated sample was removed from the vacuum chamber and fluid, excess water blotted, and weighed again to obtain the saturated mass, m_{sat}, and a THz-TDS map (19 mm x 42 mm; 0.5 mm/pixel) was collected to map the saturated pores.

The sample was centrifuged using an Eppendorf 5801 with a FA-45-6-30 fixed angle rotor to clear large pores based on the applied capillary pressure assuming a contact angle of 45° and the interfacial tension of 72.8 mN/m. Following centrifugation, the sample was weighed to obtain the centrifuged mass, m_{cent}, and another THz TDS map collected to map the micropores. Finally, the samples are oven dried at 100 °C, weighed to obtain the final dry mass, $m_{dry,f}$, and the final THz TDS spectroscopy map collected.

The full workflow was repeated two to three times per 2 mm, 4 mm, and 6 mm samples to clear pore with pore dimeter (d_p) greater than 1 μm. If samples fractured during centrifugation, the pieces were recovered from the centrifuge tube, weighed, and pieced back together for THz mapping.

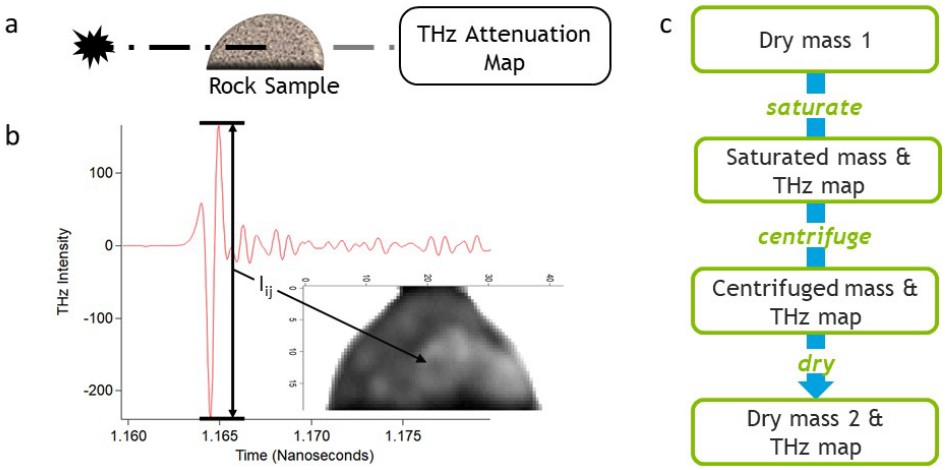

Figure 1. Schematic of the measurement scheme and workflow. (a) The Terahertz (THz) beam passes through the rock sample to produce a THz-TDS attenutiaon map. (b) The THz-TDS pulse (red) and the marked peak-to-peak amplitude (black) used to generate the attenuation map where the darkest pixels are the most attenuating and the brightest the least. (c) THz-TDS workflow.

2.3.1 Porosity and Microporosity by Mass

The mass data were used to calculate the total (ϕ_m) and microporosity ($\phi_{\mu,m}$). The total porosity was calculated as the ratio of the saturated pore volume, V_p, to the bulk volume, V_b, and V_p is calculated using the mass balance between the water saturated rock, m_{sat}, and dry rock, m_{dry}, and the density of water, ρ_w, as 1 g/cm^3.

The bulk density, ρ_b, of each sample was calculated from the mass and dimensions of each plug. The bulk density of Samples 1 and 2 is 2.2 g/cm^3 and Sample 3 is 2.3 g/cm^3.

The amount of $\phi_{\mu,\mathrm{m}}$ is determined as the ratio of the volume of micropores, $V_{\mu pores}$, to V_b where $V_{\mu pores}$ is calculated from the mass balance using the mass of the rock after centrifugation, m_{cent}, and the final dry mass of the rock, $m_{dry,f}$.

2.3.2 Microporosity by THz

While the goal of the THz imaging is not to directly calculate microporosity but to provide maps of the spatial variations in the microporosity within the sample, the sensitivity of the measurement to the water in the sample does provide a means to estimate the microporosity from THz ($\phi_{\mu,THz}$) as shown in Eqn. 1

$$\phi_{\mu,THz} = avg\left(\frac{\left(\frac{THz_{cent,ij}}{THz_{sat,ij}}\right)}{max\left(\frac{THz_{cent,ij}}{THz_{sat,ij}}\right)}\right) * avg\left(\frac{\left(\frac{THz_{sat,ij}}{THz_{dry,ij}}\right)}{\rho_b * max\left(\frac{THz_{sat,ij}}{THz_{dry,ij}}\right)}\right) \quad (1)$$

where $THz_{cent,ij}$, $THz_{sat,ij}$, and $THz_{dry,ij}$ are the THz attenuation map intensity data at each ij pixel within a region of interest (ROI) selected around the rock boundary. The maximum of the ratio of the two maps was used to account for power fluctuations that might occur due to fluctuations in the humidity of the air and changes in alignment. The relative amount of the relative amount of microporosity, $\phi_{\mu,THz}$, to total porosity from mass, ϕ_m was then calculated for comparison to mass balance and MICP.

2.4 Mercury Injection Capillary Pressure (MICP)

Remaining portions of the plugs sampled for THz imaging were used for mercury injection capillary porosimetry (MICP) analysis (MetaRock Laboratories, Houston, TX). A full description of the MICP technique and apparatus can be found in general petrophysics textbooks [12]. Plug samples were tested in the as-received state and then dried in an oven at 100 °C. The maximum pressure applied in MICP is 60,000 psi. The microporosity from MICP $\phi\mu_{,MICP}$ were obtained from the cumulative PSD curve.

2.5 X-Ray Computed Tomography (CT)

CT scans were collected using a NSI X5000 Industrial CT scanner (North Star Imaging, Inc.) to observe the grain and large pores within the remaining half-plugs used for MICP. The scans were performed at 720 views per rotation where the reconstructed voxel size was 50 µm x 50 µm x 50 µm. The CT radiographs were reconstructed using the iTomoFDK software (iTomography Corporation, Houston, TX). GeoDict (Math2Market) was used to generate 3D renderings of the CT scans and segment the large pores using a simple intensity cutoff.

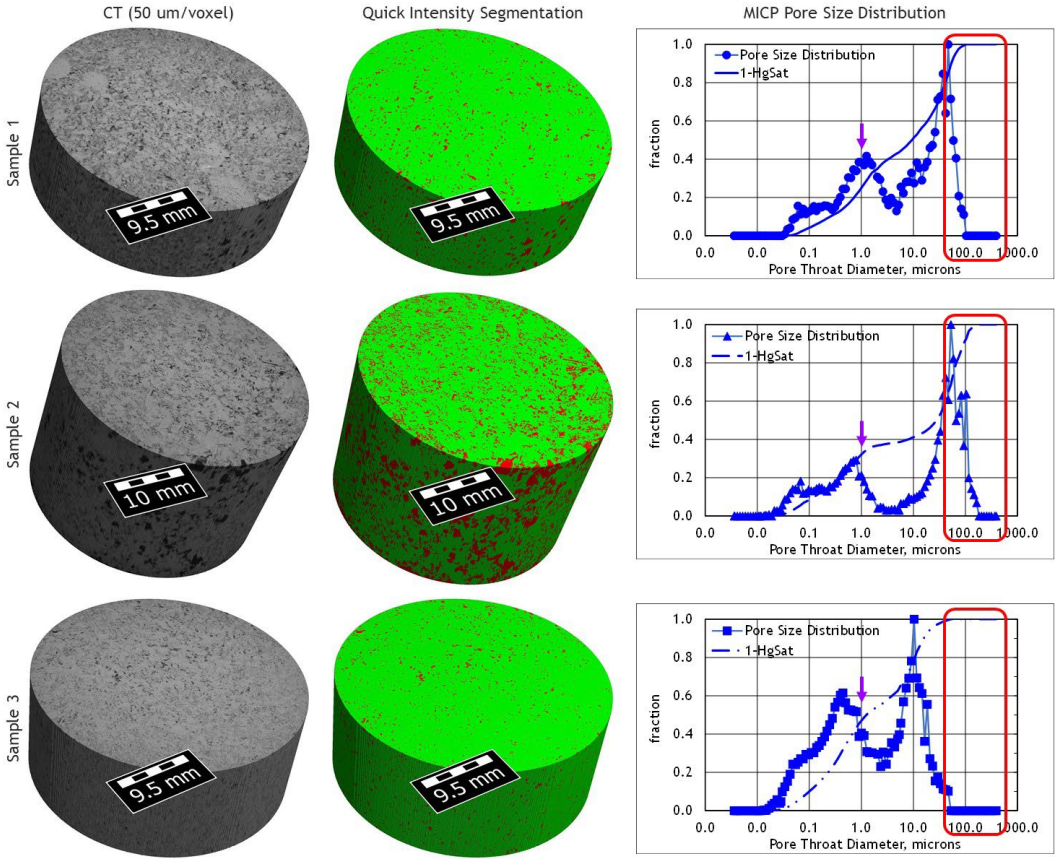

Figure 2. X-Ray CT Scans and MICP Pore Size Distributions. (left) CT scan renderings of the portions of each sample used for MICP analysis The black to dark grey voxels are large pores and the light grey voxels contain matrix minerals and unresolved pores. (middle) Segmented CT scans showing resolvable pores (red) with pore sizes larger than the voxel size (50 µm x 50 µm x 50 µm). (right) Normalized PSD and cumulative curves from MICP. Red box indicates the approximate pore size range of the segemented pores and the purple arrows indicate the pore size cutoff for micropores (d_p < 1 µm).

3 Results and Discussion

3.1 THz Maps

Figure 2 shows CT scans of the samples used for MICP analysis in grayscale and segmented to show large pores. The normalized PSD obtained by MICP from each sample is also shown where the red box indicates the approximate range of pore sizes resolvable in the CT reconstructions. The MICP data confirm that few pores in the sample are on the order of 10s of microns and the relative amount of micropores with d_p smaller than 1 µm varies between 20% and 50% of the total porosity (see also Figure 5).

Figure 3 shows a photo, THz TDS attenuation maps, and THz TDS difference maps of the 4mm thick section of Sample 2. The color variations in the photo (Fig. 3a) are due to variations in mineralogy, cementation, porosity, and surface roughness.

The attenuation maps shown in Fig. 3b-3d show grayscale intensity variations which change with the presence of water, scattering, and to a lesser extent with the rock composition. Thus, the darkest pixels in the saturated (Fig. 3b) and centrifuged (Fig. 3c) maps are those that contain the most water where the intensity variations in the dry map (Fig. 3d) are related to compositional and structural variations. Edge artifacts, visible as a high-intensity ring along the edge of the sample in Figs. 3b-3d, are caused by the knife edge effect wherein the sharp edge of the sample causes some radiation to diffract around it and blurs the THz signal.

The difference maps in Figures 3e-3g show how the attenuation changed between steps. The areas of the difference map comparing the saturated versus dry attenuation maps (Fig. 3e) shows the regions of the sample that became saturated with water upon vacuum saturation. Similarly, the areas of difference maps comparing the saturated versus centrifuged attenuation maps (Fig. 3f) shows the regions of the sample that lost the most water during centrifugation, meaning those containing the pores larger than the cutoff (i.e., macropores). The areas of the difference map comparing the centrifuged versus dry attenuation maps (Fig. 3g) shows the regions of the sample that lost water during drying, meaning those regions containing the pores smaller than the cutoff (i.e., micropores). When

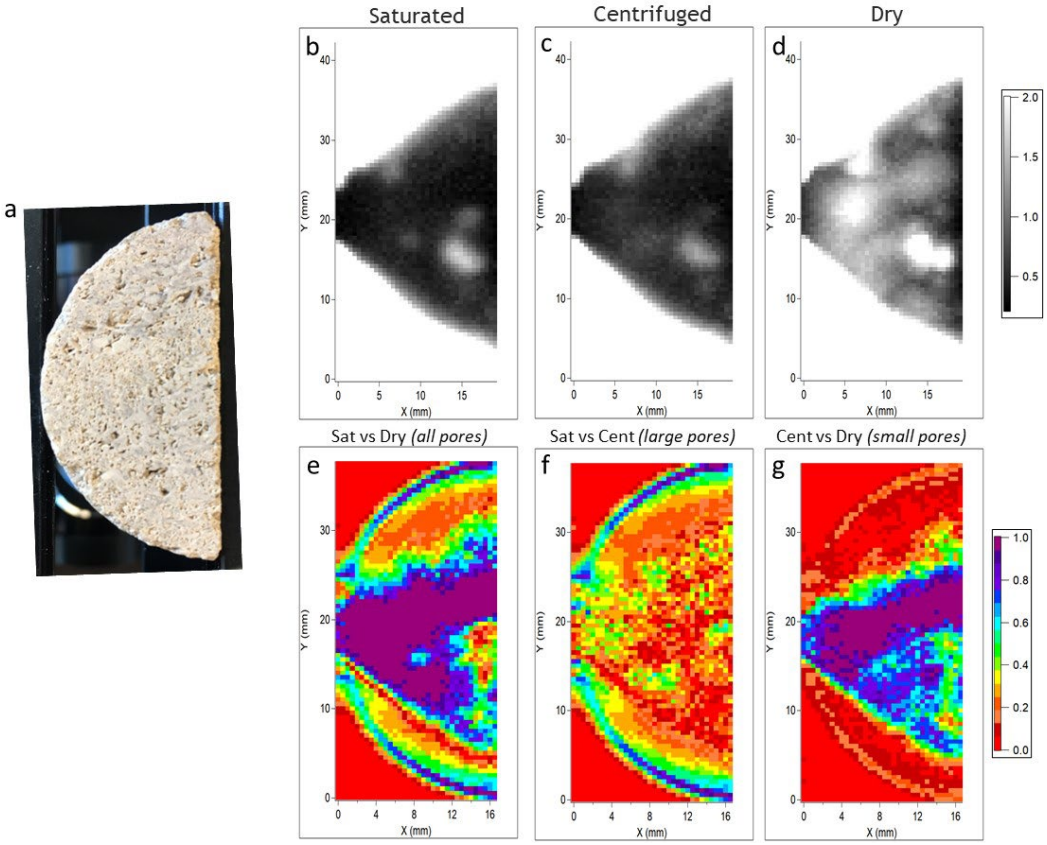

Figure 3. THz-TDS attenuation and attenuation difference maps of Sample 2 (4 mm thick) as representative data examples. (a) photo, (b-d) normalized attenuation maps of the saturated, centrifuged, and dry samples, and (e-g) difference maps between the saturated and dry, saturated, and centrifuged, and centrifuged and dry attenuation maps to represent the spatial variation of the saturated pores, macropores (d_p > 1 µm), and micropores (d_p < 1 µm).

comparing each of the difference maps, in Fig. 3e-3g, the locations of the macro- and micropores can be seen. In this example there appears to be a clear band of micropores through the center of the sample (Fig. 3g) whereas the macropores are more evenly distributed (Fig. 3f).

Figure 4 shows the photos and macroporosity and microporosity maps for all three samples. The maps show how the distribution of macro- and micropores vary in each of the samples. Sample 1 shows a concentration of micropores in the center of the sample (green and purple pixels) and concentrated micropores on the left. Sample 2 shows distributed macropores (orange, yellow, and green pixels) and a concentrated band and patches of micropores. Finally, Sample 3 shows distributed macro- and micropores. In each case the THz difference maps indicate regions of co-localized macro- and micropores as would be expected for carbonate rocks. Sample 3 appears to have more co-localization of the macro- and micropores where Sample 1 has less, and Sample 2 has the least. This will be confirmed in future work with thin section and high-resolution imaging studies of these samples.

3.2 Porosity and Microporosity Comparisons

Figure 5 compares the measured porosity and microporosity for each sample. The total porosity was measured on the half-plugs by MICP and on the THz samples by mass balance (mass) (Fig. 5a). The microporosity below the d_p = 1 µm (purple data) pore clearing cutoff (Fig. 5a) was measured on the THz samples by mass balance (mass) and from the THz maps using Eqn. 1 (THz), and on half-plugs by MICP (MICP). Figure 5b shows the relative amount of the total porosity that is microporosity from the mass balance (mass) and THz maps on the THz sample (THz) compared to what was measured by MICP on half-plugs (MICP) for the d_p = 1 µm (purple data) pore clearing cutoff. The mass balance and THz porosity and microporosity data are the average of the measurements and the error bars are one standard deviation. The mass balance and THz maps are measured on the same half-moon samples and include the 2mm, 4mm, and 6mm thick samples where the MICP data was measured on a half plug.

The porosity data (Fig. 5a) shows that the total porosity of the samples ranges from 20% to 17% and decreases from Sample 1 with the highest to Sample 3 with the lowest total porosity. Comparisons of the dry mass before and after each run showed some mass loss during the process

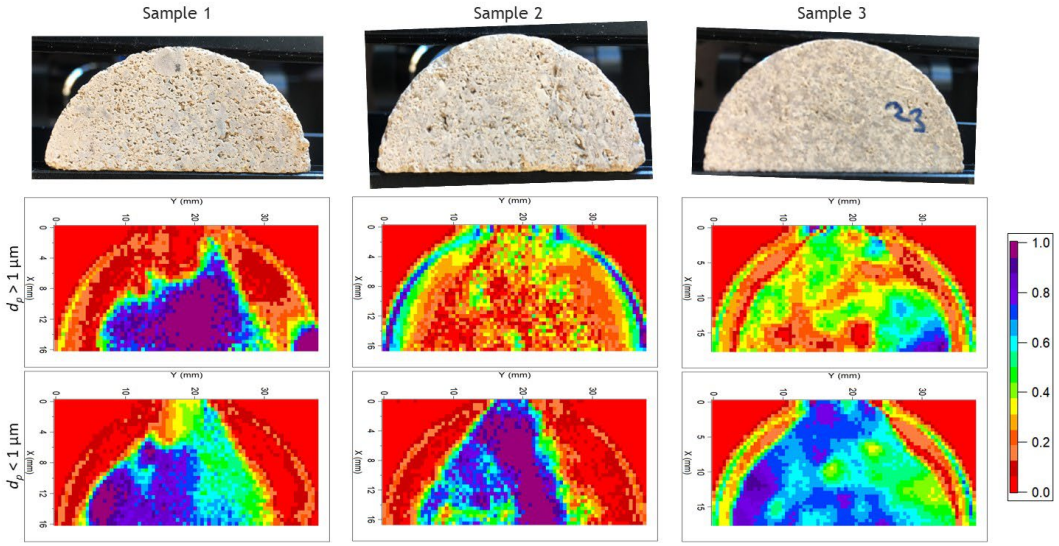

Figure 4. THz-TDS attenuation difference maps of each sample (4 mm thick) showing macro- and microporosity. (top) photo, (middle) macropores ($d_p > 1$ µm), and (bottom) micropores ($d_p < 1$ µm).

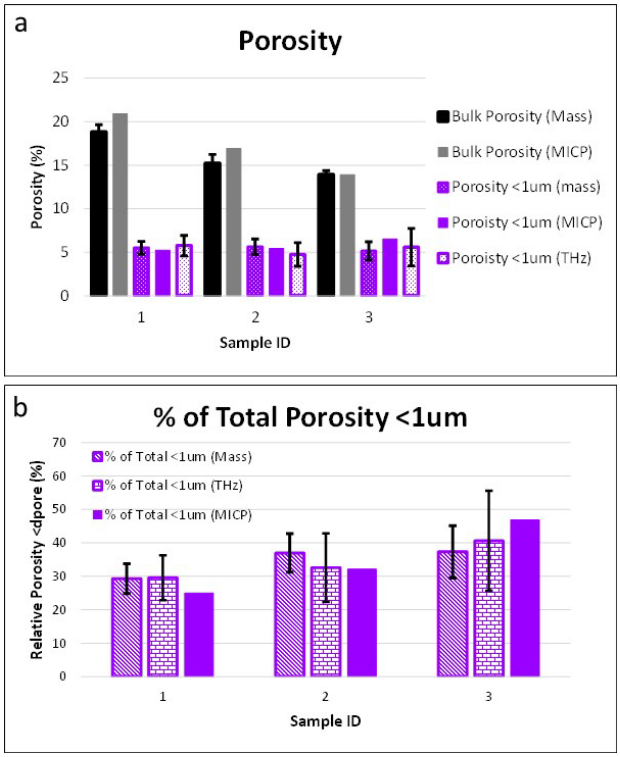

Figure 5. Porosity and microporosity comparisons. (a) Total porosity and microporosity for Samples 1-3. Total porosity from MICP (grey) and mass balance (black). The microporosity with dp <1 µm from mass balance (white dots), MICP (solid), and THz-TDS maps (purple dots). (b) Relative amount of the total porosity attributed to the microporosity with d_p <1 µm from mass (diagonal lines), THz-TDS (brick), and MICP (solid). In both (a) and (b), the THz and mass data are the average of data collected on the half mood samples and the error bars represent one standard deviation.

which was attributed to erosion processes and potential loss of mechanical stability of small pores and rock material along the boundaries. Despite this, the comparison between the porosity and relative amount of microporosity measured for $d_p > 1$ µm pore clearing threshold are in excellent agreement between all methods, mass balance, THz maps, and MICP (Fig. 5a and 5b).

4 Conclusions

This paper demonstrates the use of THz TDS to map pore structure heterogeneity in carbonate rocks using the THz attenuation due to water-filled pores. Three carbonate rocks with varying ϕ and PSD were used to demonstrate the effectiveness of the method. When the samples are centrifuged to selectively displace water with air in pores larger than a selected pore size threshold, the THz TDS maps provide a unique capability to map large field-of-view ϕ_μ distributions (Fig. 3 and Fig. 4) within these bimodal pore systems.

The workflow presented also demonstrates the ability to quantify the percentage of the ϕ_μ using the data obtained from the THz and mass balance on the samples (Fig. 5). When compared to total and microporosity distributions obtained from MICP the results from the presented workflow are in good agreement.

In summary, the workflow presented in this paper provides a first demonstration of using THz TDS to map and quantify ϕ_μ in carbonate rocks which have a bimodal pore size distribution and contain a significant amount of ϕ_μ. Thus, given the excellent agreement between the relative amount of microporosity at $d_p < 1$ µm, the threshold for formation evaluation, obtained by the THz TDS workflow compared with that from MICP and the added ability to map microporosity spatial variations, we believe that this workflow provides valuable information for future incorporation into special core analysis workflows.

Acknowledgements

We would like to thank Ayrat Gizzatov, Gary Eppler, and Qiushi Sun for their help with sampling, sample preparation, and CT scanning.

References

1. Chopra, S., N. Chemingui, and R.D. Miller, The Leading Edge, **24** 488-489 (2005).
2. Schön, J.H., *Physical properties of rocks: Fundamentals and principles of petrophysics*. 2015: Elsevier.
3. Cantrell, D.L. and R.M. Hagerty, GeoArabia, **4** 129-154 (1999).
4. Clerke, E.A., SPE Journal, **14** 524-531 (2009).
5. Patzek, T.W., A.M. Saad, and A. Hassan, Energies, **15** 1243 (2022).
6. Pittman, E.D., AAPG Bulletin, **55** 1873-1878 (1971).
7. Stanley, R., S. Guidry, and H. Al-Ansi. *Microporosity spatial modeling in a giant carbonate reservoir*. in *International Petroleum Technology Conference*. 2015. OnePetro.
8. Ibrahim Khan, M. and M.R. Islam, *The Petroleum Engineering Handbook: Sustainable Operations*. 2007: Gulf Publishing Company.
9. Baker, R.O., H.W. Yarranton, and J.L. Jensen, *Practical Reservoir Engineering and Characterization*. 2015: Gulf Professional Publishing.
10. Ramsey, M., Schlumberger., (2019).
11. Conner, W., et al., Langmuir, **2** 151-154 (1986).
12. Dandekar, A.Y., *Petroleum reservoir rock and fluid properties*. 2013: CRC press.
13. Funk, J., et al. *Core imaging—twenty five years of equipment, techniques, and applications of X-ray computed tomography (CT) for core analysis*. in *International Symposium of the Society of Core Analysts*. 2011.
14. Heshmat, B., et al., Optics express, **25** 27370-27385 (2017).
15. Tiab, D. and E.C. Donaldson, *Petrophysics: theory and practice of measuring reservoir rock and fluid transport properties*. 2015: Gulf professional publishing.
16. Singh, K., et al., Scientific data, **5** 1-8 (2018).
17. Zhang, Y., et al., Fuel, **207** 312-322 (2017).
18. Hackley, P.C., et al., International Journal of Coal Geology, **241** 103745 (2021).
19. Hurley, N.F., K. Nakamura, and H. Rosenberg, Journal of Sedimentary Research, **91** 735-750 (2021).
20. Jobe, T., et al., Petroleum Geoscience, **24** 323-334 (2018).
21. Jobe, T.D., *Sedimentology, chemostratigraphy and quantitative pore architecture in microporous carbonates: Examples from a giant oil field offshore Abu Dhabi, UAE*. 2013: Colorado School of Mines.
22. Pahlevaninezhad, H., B. Heshmat, and T.E. Darcie, IEEE Photon, **3** 307-310 (2011).
23. Redo-Sanchez, A., et al., Nature Communications, 12665 (2016).
24. Heshmat, B., et al., Nano Letters, **12** 6255-6259 (2012).
25. Heshmat, B., H. Pahlevaninezhad, and T.E. Darcie, IEEE Photonics Journal, **4** 970-985 (2012).
26. Walther, M., et al., Analytical and Bioanalytical Chemistry, 1009-1017 (2010).
27. Abraham, E., et al., Applied Physics A, **100** 585-590 (2014).
28. Fukunaga, K. and M. Picollo. *Terahertz time domain spectroscopy and imaging applied to cultural heritage*. in *13th International Symposium on Nondestructive Characterization of Materials*. 2013. Le Mans, France.
29. Banerjee, D., et al., Optics express, **16** 9060-9066 (2008).
30. Castro-Camus, E., M. Palomar, and A. Covarrubias, Scientific reports, **3** 1-5 (2013).
31. Wang, Y., et al., Optics Express, **18** 15504-15512 (2010).
32. Kemp, M., et al. *Security applications of terahertz technology*. in *AeroSense 2003*. 2003. Orlando, Florida.
33. Bawuah, P., et al., Journal of Infrared, Millimeter, and Terahertz Waves, **41** 450-469 (2020).
34. Naftaly, M., et al., MDPI Sensors, **20** (2020).